

Chapter 6

EFFECTS OF BUBBLES ON THE ELECTROCHEMICAL BEHAVIOR OF HYDROGEN-EVOLVING SI MICROWIRE ARRAYS ORIENTED AGAINST GRAVITY

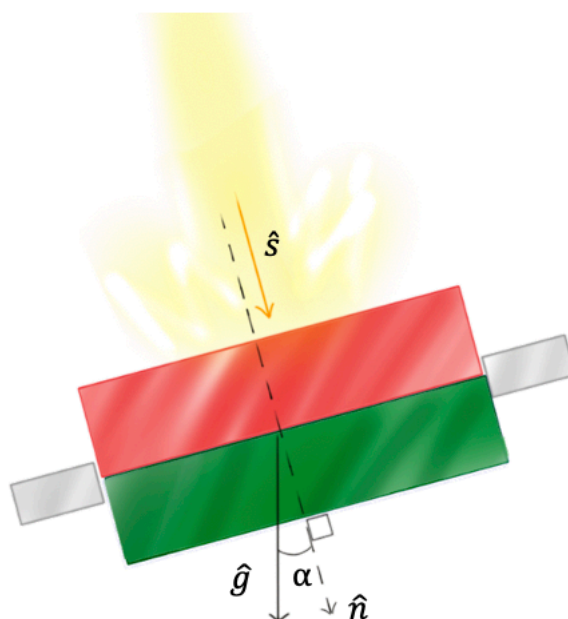
Kempler, P.A., Coridan, R.H., Lewis N.S. (2020). Effects of Bubbles on the Electrochemical Behavior of Hydrogen-Evolving Si Microwire Arrays Oriented Against Gravity. *Energy & Environmental Science*, 13, 1808-1817.

<https://doi.org/10.1039/D0EE00356E>

6.1 Introduction

Studies of the hydrogen-evolution reaction (HER) have provided a detailed understanding of the nucleation and growth behavior of individual $\text{H}_2(\text{g})$ bubbles.^{4, 16-18} Capillary forces at structured electrode surfaces provide a mechanism for reducing the adhesive force of gas bubbles. Moreover, “aerophobic” electrodes prepared from nanostructured metals and light absorbers effect a reduction in the diameter of departing bubbles due to increased wettability of the surface.¹⁹⁻²¹ Photoelectrochemical H_2 evolution from an InP photocathode modified with nanostructured Rh has been investigated in a microgravity environment,²² and under simulated sunlight yielded $|j_{\text{H}_2}| > 14 \text{ mA cm}^{-2}$ for 9 s in 1.0 M HClO_4 containing 1% (v/v) isopropyl alcohol. Si microwire, μW , array electrodes exhibit a low gas coverage during H_2 evolution due to the increased wettability of the surface relative to a planar Si electrode.²³ Tandem device designs evolving separate

streams of combustible gases require at least one downward-facing electrode, generating either H_2 or O_2 (**Scheme 6.1**), but the effects of electrochemical generation of gases at rates relevant to efficient solar fuels generation, while opposing gravity and without external forced convection, are not well understood. Vertically oriented Si μW arrays, having diameters approximately equal to the minority-carrier diffusion length and having heights large enough to be embedded in ion-conducting membranes, are a technologically-relevant model system for studies of gas evolution in integrated solar fuels generation systems.²⁴



Scheme 6.1: Monolithic, integrated tandem solar fuels device, with a wide band-gap semiconductor represented in red, a narrow band-gap semiconductor represented in green, embedded in a gray membrane for product separation. The orientation, α , is defined as the angle between the gravitational vector and the surface normal of the bottom side of the device. Optimal solar collection occurs when $\hat{n} \cdot \hat{s}$ approaches 1. The path of current-carrying charged species is represented as a dotted line.

We report herein the electrochemical behavior of representative planar and microwire-array cathodes prepared from n^+ -Si(100) surfaces metalized with a continuous layer of Pt, to understand how the geometry and orientation of these electrodes control the size-distribution and coverage of $H_2(g)$ bubbles. Moreover, the effects of H_2 evolution on the electrochemical behavior of the dark, downward-facing side of an integrated solar-driven water-splitting device, including effects on mass transport-limited current densities, the concentrations of dissolved H_2 near the electrode surface, and resistance drops at the cathode, have been elucidated through extensive measurements of bubble size distributions and coverages.

6.2 Experimental Methods

Fabrication of electrodes: Microstructured Si substrates were prepared as described in the Appendix (A.1). Metallization was performed in an Orion Series Sputtering system (AJA) at a base pressure of 10^{-7} torr. Ti and Pt films were sputtered sequentially in a 5 mtorr Ar plasma at a deposition rate of $\sim 1 \text{ nm min}^{-1}$ and $\sim 2.6 \text{ nm min}^{-1}$, respectively. An ohmic back contact was made to the rear side of the Si with an In-Ga eutectic (Alfa Aesar), and the electrode was affixed to a Cu-Sn wire via conductive Ag epoxy (Ted Pella). The electrode was sealed into a piece of 6 mm diameter borosilicate glass tubing using a chemically resistant epoxy (Hysol 9460) that was cured for >12 h at room temperature. The electrode area was measured using a commercial optical scanner.

Electrochemical measurements: HER characteristics were evaluated in a 4-port electrochemical cell that contained an optical flat at the base of the cell to facilitate viewing of the electrode. Degenerately doped n^+ -Si electrodes were used to eliminate the effects of a photoactive substrate and to evaluate the performance under conditions experienced by a

downward-facing, dark electrode, where gas coverage does not affect light absorption. The electrolyte was 0.50 M $\text{H}_2\text{SO}_4(\text{aq})$ (TraceMetal Grade, Fisher) that was purged with $\text{H}_2(\text{g})$ for at least 30 min prior to testing, and was purged between experiments to maintain $\text{H}_2(\text{aq})$ in equilibrium with $\text{H}_2(\text{g})$ at 1 atm. A saturated calomel electrode served as the reference electrode and a Pt mesh electrode behind a Nafion (Dupont) membrane served as the counter electrode. A constant current or potential was obtained using a Biologic SP-200 potentiostat. The cell was mounted on a leveled surface and the electrode orientation was varied by tilting the electrochemical cell to match the angle defined by custom shims.

Macroscopic video collection and analysis: The gas coverage and the size distribution of bubbles were analyzed from video acquired at 60 frames s^{-1} , at a pixel width of 300 μm , using a commercially available high-definition camera mounted on optical posts (Thorlabs). Videos were recorded under illumination provided by a filtered Hg (Xe) lamp. Images were processed in MATLAB. Image thresholding was used to estimate the fractional gas coverage, θ , with black pixels representing the electrode and white pixels representing regions covered by gas bubbles. Bubble size distributions were measured as circles detected within individual images processed via a Hough transform of the grayscale image. Statistics were acquired after at least 2 min of continuous H_2 evolution to allow the behavior of the electrode to stabilize. Large bubbles could not be automatically detected and were therefore measured manually. Bubbles with diameters $< 300 \mu\text{m}$ (~ 10 pixels) were omitted from macroscale measurements.

Microscopic video collection and analysis: High-speed microscopy experiments were performed in 0.50 M $\text{H}_2\text{SO}_4(\text{aq})$ in an HDPE electrochemical cell with a glass cover. The imaging system consisted of a microscope (Olympus BX-53) with a 5x objective, an LED

reflectance illuminator (Prior Scientific), and a high-speed camera (Fastec Imaging). All imaging experiments were performed at 200 frames per second. Bubble radii were measured through extended image sequences using routines developed from the SciPy and Scikit-Learn libraries for the Python programming language.

6.3 Results

Figure 6.1 presents scanning-electron micrographs of n^+ -Si microwire arrays after metallization with Ti/Pt. Deep reactive-ion etching of patterned n^+ -Si(100) surfaces produced μ W arrays over cm^2 areas with the microwires highly uniform in diameter, pitch, and height. Deposition of Pt by sputtering did not substantially modify the geometry or surface roughness of the array. Arrays were etched to a height of 30 μm , and three array geometries: (as defined by the photolithographic mask and etching time; 6 μm diameter and 14 μm center-to-center pitch, μW 6|14; 6 μm diameter and 28 μm pitch, μW 6|28; and 3 μm diameter and 11 μm pitch, μW 3|11) were prepared to investigate the electrochemical effects of variation in microwire spacing and diameter. The diameters and pitches of the arrays were measured via scanning electron microscopy of representative cross sections of the array and were consistent with the predicted dimensions.

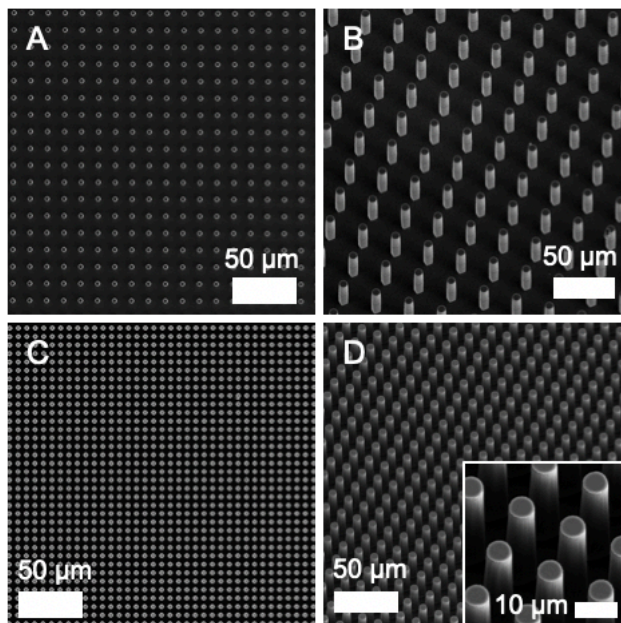


Figure 6.1: Scanning electron microscope images of platinized n^+ -Si(100) microwire arrays of nominal diameter 6 μm , height 30 μm , and pitch 28 μm (A,B) and 14 μm (C,D). Images acquired at normal incidence (A,C), scale bar represents 100 μm ; 30 degrees of tilt (B,D) scale bar represents 50 μm , inset scale bar represents 10 μm .

6.3.1 Electrochemical behavior of inverted cathodes

The electrochemical behavior of planar and microstructured n^+ -Si/Ti/Pt cathodes were compared in a stagnant cell containing 0.50 M $\text{H}_2\text{SO}_4(\text{aq})$. Figure 5.2 displays the time-dependent overpotential, η_T , of planar and microstructured n^+ -Si/Ti/Pt cathodes as a function of current density, J , and orientation, α , with α representing the angle between the gravitational vector and the surface normal of the bottom side of the electrode. At acute angles of α (i.e., predominantly downward-facing electrodes) planar n^+ -Si/Ti/Pt electrodes exhibited large η_T relative to the reversible hydrogen potential, RHE, to drive a constant J for the HER, J_{H_2} . The increase in η_T was proportional to the current density, and abrupt decreases in η_T with time correlated with the periodic release of large gas bubbles from

the electrode surface (Figure 5.2B). In contrast, despite the generation of gas bubbles, n^+ -Si/Ti/Pt microwire array electrodes exhibited stable, and much lower, values of η_T under chronoamperometric control. Downward-facing ($\alpha \sim 0^\circ$) microwire array and planar electrodes at $|j_{H_2}| < 30 \text{ mA cm}^{-2}$ trapped large gas bubbles and exhibited potentials that were unstable with time, but also showed potentials that were lower on average than the potential exhibited by the same electrode when facing upwards ($\alpha = 180^\circ$).

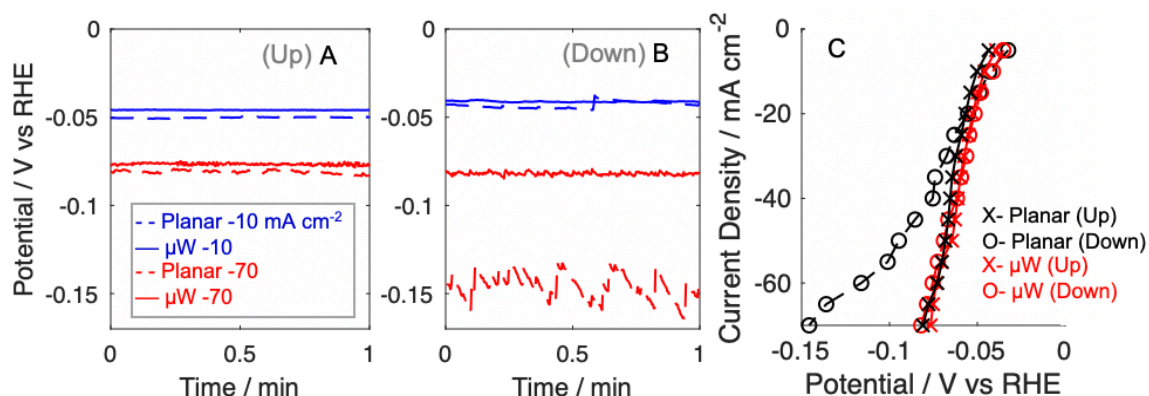


Figure 6.2: Comparison of the (A) upward-facing and (B) downward-facing electrochemical behavior of galvanostatically controlled planar and microstructured cathodes, respectively, in 0.50 M $H_2SO_4(aq)$ as a function of current density. Planar Pt electrodes are represented by dashed lines and μW 6|14 electrodes are represented by continuous lines. Devices behaved mutually similarly when facing upward but at high current, inverted planar Pt exhibited increased overpotentials relative to microstructured electrodes. (C) Comparison of the average potential required to produce a constant current density at a planar Pt electrode, black, and a μW 6|14 electrode. Upward-facing behavior is represented by x's, whereas downward-facing behavior is represented by open circles.

6.3.2 Physical characterization of bubble films

To investigate the role of gas coverage on fluctuations in the overpotential, electrochemical experiments were performed in tandem with macroscopic and microscopic imaging of the electrode surface. Figure 5.3 shows changes in the fractional gas coverage,

θ , as a function of time for n^+ -Si/Ti/Pt electrodes held at $J = -30 \text{ mA cm}^{-2}$. Inverted ($\alpha = 15^\circ$) planar n^+ -Si/Ti/Pt electrodes exhibited a time-dependent value of θ that was positively correlated with the absolute overpotential relative to RHE (Figure 5.3A), with greater changes in η_T occurring at larger $|J_{H_2}|$. In contrast, regardless of orientation, microstructured n^+ -Si/Ti/Pt electrodes exhibited stable η_T and θ values over time (Figure 5.3B-D). The average value of θ at a given $|J_{H_2}|$ was a function of the geometry of the n^+ -Si/Ti/Pt microwire array. At $|J_{H_2}| = 30 \text{ mA cm}^{-2}$, $\mu\text{W } 6|14$ electrodes exhibited an average $\theta = 15\%$, whereas $\mu\text{W } 3|11$ and $\mu\text{W } 6|28$ electrodes exhibited an average $\theta = 41\%$ and 52% , respectively. Despite the variation in θ for electrodes of different microwire array geometries, values for η_T were relatively insensitive to the μW array geometry, indicating that gas coverage alone was not a strong predictor of the chronopotentiometric behavior (Figure 5.2B-D). Notably, $\mu\text{W } 6|28$ cathodes maintained low overpotentials for the HER despite having gas coverages comparable to those of planar n^+ -Si/Ti/Pt electrodes. For planar, $\mu\text{W } 3|11$, and $\mu\text{W } 6|28$ electrodes, θ increased asymptotically as $|J_{H_2}|$ increased, although the stable value of θ depended on the microstructure of the electrode.

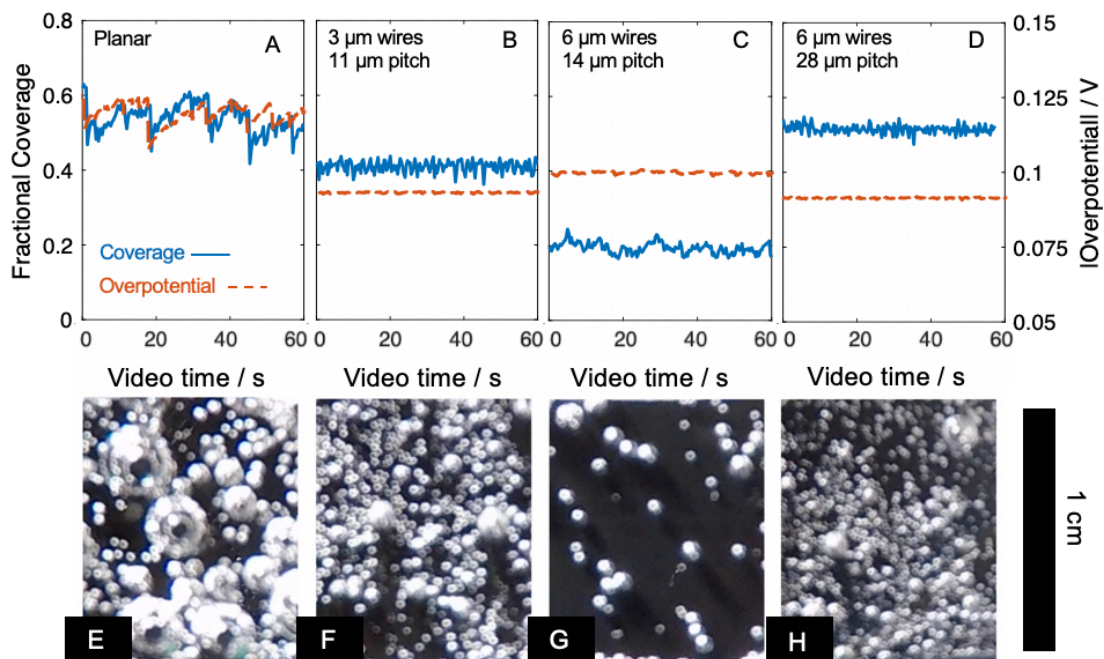


Figure 6.3: (A-D) Comparison of fractional gas coverage of downward-facing n^+ -Si/Ti/Pt cathodes, at $\alpha = 15^\circ$, at -30 mA cm^{-2} in $0.50 \text{ M H}_2\text{SO}_4(\text{aq})$, relative to the absolute overpotential for the HER in $0.50 \text{ M H}_2\text{SO}_4(\text{aq})$ as a function of time. (E-H) Representative images from videos recorded at 60 frames s^{-1} of downward-facing cathodes passing a current density of 30 mA cm^{-2} for the HER. (A,E) planar n^+ -Si(100); Si microwire arrays with a width and pitch, respectively of: (B,F) 3 and 11 μm ; (C,G) 6 and 14 μm ; and (D,H) 6 and 28 μm . Scale bar represents 1 cm.

The primary difference between the gas bubble layer that covered μW and planar n^+ -Si/Ti/Pt electrodes was the size of the bubbles (**Figure 6.3E-H**). The weighted mean diameter, \bar{d}_w , of a gas bubble film is calculated from **Equation 6.1**, where each bubble is weighted its respective projected area.

Figure 6.4 compares $\langle d_w \rangle$, for various n^+ -Si/Ti/Pt electrodes at $\alpha = 15^\circ$ as a function of $|J_{H_2}|$. At $\alpha = 15^\circ$ and $|J_{H_2}| = 30 \text{ mA cm}^{-2}$, $\langle d_w \rangle$, at planar n^+ -Si/Ti/Pt electrodes

varied between 0.5 and 3 mm, whereas $\langle d_w \rangle$, was consistently < 0.6 mm at $\mu\text{W } 6|14$ and $\mu\text{W } 3|11$ electrodes. The variation in θ for different microwire array geometries was caused by a difference in the number density of bubbles, N , as opposed to a difference in the size of the bubbles adhering to the surface (**Figure 6.4E-G**).

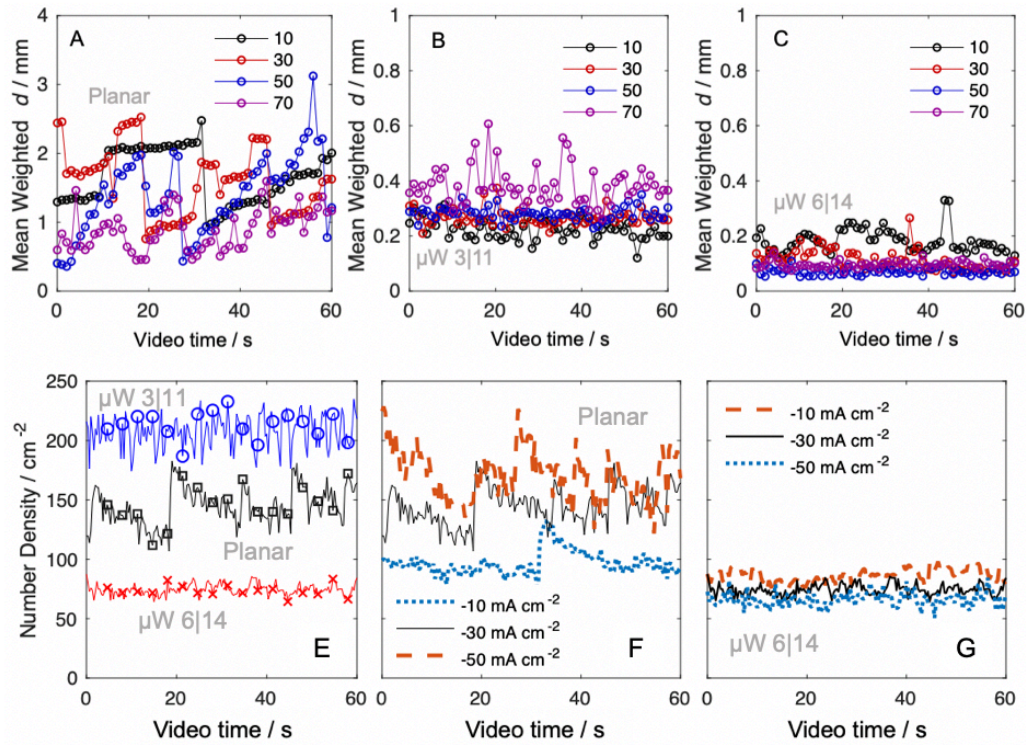


Figure 6.4: (A-C) Weighted mean bubble diameters (**Equation 6.1**) versus video time at $|J_{H_2}| = 10\text{--}70 \text{ mA cm}^{-2}$ as measured at (A) $\text{n}^+\text{-Si/Ti/Pt}$ planar, (B) $\mu\text{W } 3|11$, and (C) $\mu\text{W } 6|14$ electrodes in $0.50 \text{ M H}_2\text{SO}_4(\text{aq})$ at $\alpha = 15^\circ$. (E-G) Number density, N , of bubbles on the electrode surface as a function of time for planar, $\mu\text{W } 6|14$, and $\mu\text{W } 3|11$ $\text{n}^+\text{-Si/Ti/Pt}$ electrodes passing -30 mA cm^{-2} in $0.50 \text{ M H}_2\text{SO}_4(\text{aq})$ at $\alpha = 15^\circ$ represented by black squares, red x's and blue circles respectively. Number density of bubbles on a (F) planar and (G) $\mu\text{W } 6|14$ $\text{n}^+\text{-Si/Ti/Pt}$ electrode as a function of time and absolute current density towards H_2 .

Increasing $|J_{H_2}|$ at inverted, planar $\text{n}^+\text{-Si/Ti/Pt}$ electrodes led to lower, more stable $\langle d_w \rangle$, due to a greater N on the surface, whereas for $|J_{H_2}| \leq 50 \text{ mA cm}^{-2}$, inverted $\mu\text{W } 6|14$

electrodes exhibited a bubble number density that was essentially independent of the applied current density (**Figure 6.4G**). The number density and weighted mean diameter were stable for 16 h of testing at -30 mA cm^{-2} .

To investigate the mechanism behind differences in N as a function of microstructure, the detachment and growth behavior of gas bubbles were measured via high-speed microscopy on upward-facing electrodes. **Figure 6.5** presents the growth and detachment behavior for bubbles released from an upward-facing $\mu\text{W } 6|14$ and $\mu\text{W } 6|28$ electrodes during 15 s of hydrogen evolution at $|J_{\text{H}_2}| = 50 \text{ mA cm}^{-2}$. In contrast to downward-facing electrodes, upward-facing $\mu\text{W } 6|28$ electrodes exhibited low N and θ values. On upward-facing electrodes, the mean departure diameter was not a function of the spacing between microwires, with mean departure diameters at a $\mu\text{W } 6|14$ and $\mu\text{W } 6|28$ electrode having values of $370 \pm 150 \text{ }\mu\text{m}$ and $330 \pm 170 \text{ }\mu\text{m}$, respectively (**Figure 6.5**). Repetitive nucleation was frequently observed at locations on the electrode surface that also exhibited large departure diameters. For bubble growth that is limited by radial transport of $\text{H}_2(\text{aq})$ to the surface, the radius, R , of a bubble as a function of time, t , is given by $R(t) = \tilde{b}(Dt)^{1/2}$, where D is the diffusion coefficient of the gas and \tilde{b} is the dimensionless growth coefficient.¹⁶

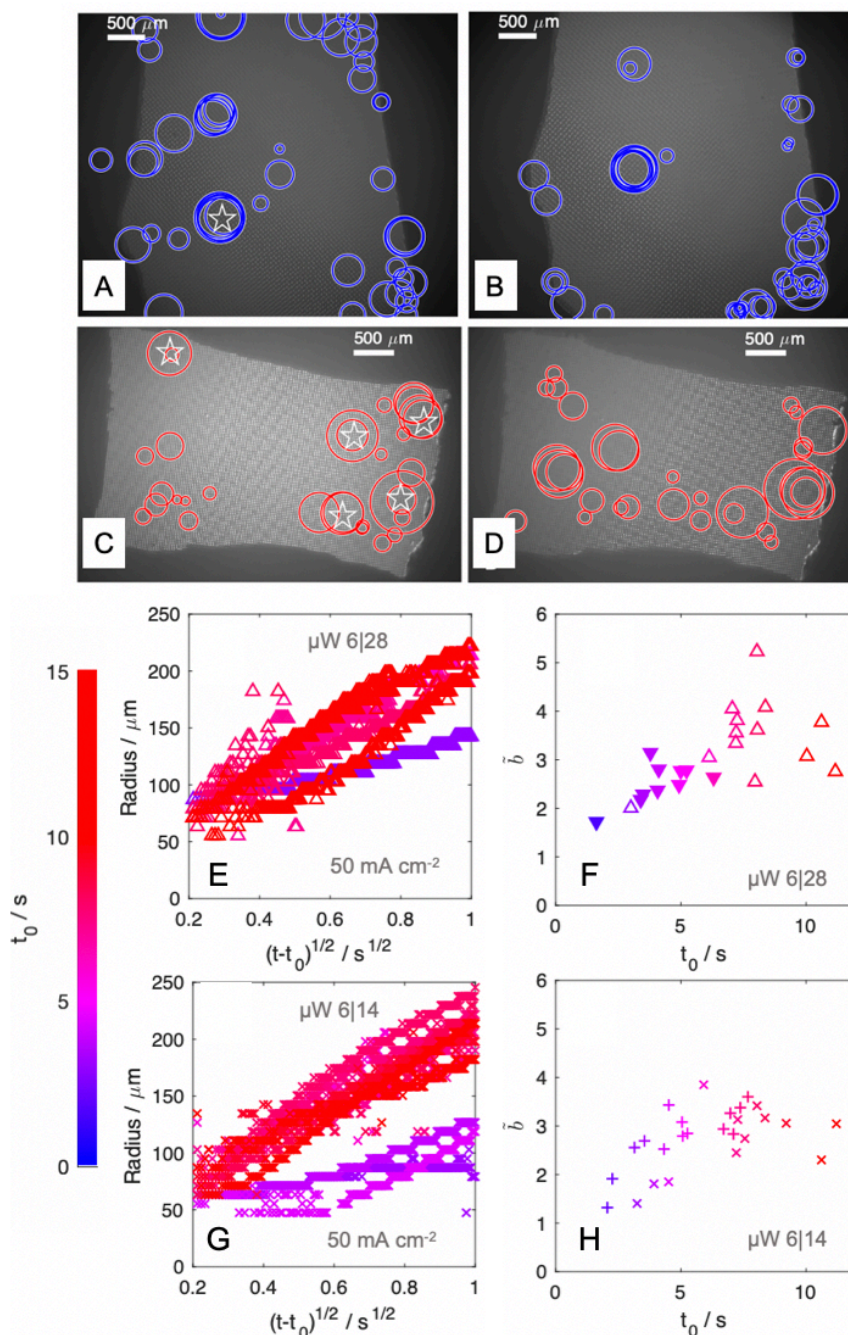


Figure 6.5: (A-D) Map of departure diameters measured during a two separate high-speed microscopy experiments at upward-facing (A-B) μW 6|14 and (C-D) μW 6|28 electrodes held at -50 mA cm^{-2} for 20 s in 0.50 M H_2SO_4 (aq). (A). (E, G) Representative radius versus square-root time traces measured via image processing software, with sites labeled in (A,C). (F,H) Calculated \tilde{b} for data presented in (E,G).

At $|J_{H_2}| = 50 \text{ mA cm}^{-2}$, values of \tilde{b} indicated that bubble growth velocities were controlled by diffusion and were stable at individual sites after 10 s (**Figure 6.5G-H**). New nucleation sites continued to form throughout the 20 s measurement, indicating that nucleation was adequately described by classical heterogeneous nucleation theory and the formation of bubbles was thus not limited to preexisting gas cavities.³⁰

6.3.3 *Mass transport properties of bubble films*

The effects of gas evolution on the mass-transport properties of inverted cathodes at $\alpha = 15^\circ$ were investigated by use of a redox-active species, ferric sulfate, as $\text{Fe}^{3+}(\text{aq})$, as a probe (**Figure 6.5A, A.6**). Following a 10 min bulk electrolysis at fixed total current density, the total quantity of $\text{Fe}^{3+}(\text{aq})$ that was reduced to $\text{Fe}^{2+}(\text{aq})$ was determined spectroscopically (**Figure A.6.2**). In the absence of both $|J_{H_2}|$ and external convection, $|J_{Fe}|$ decayed to $< 0.5 \text{ mA cm}^{-2}$ within 45 s (**Figure A.6.3**). At gas-evolving electrodes, the mean mass-transport-limited current density vs time for $\text{Fe}^{3+}(\text{aq})$ reduction, $|J_{Fe}|$, was proportional to $|J_{H_2}|$ but the response depended on the electrode surface (**Figure 6.6B**). Larger $|J_{Fe}|$ values were observed for $\mu\text{W n}^+\text{-Si/Ti/Pt}$ surfaces relative to planar $\text{n}^+\text{-Si/Ti/Pt}$ electrodes, regardless of the gas coverage. $\mu\text{W 6|28}$ electrodes exhibited the largest $|J_{Fe}|$ values at all current densities.

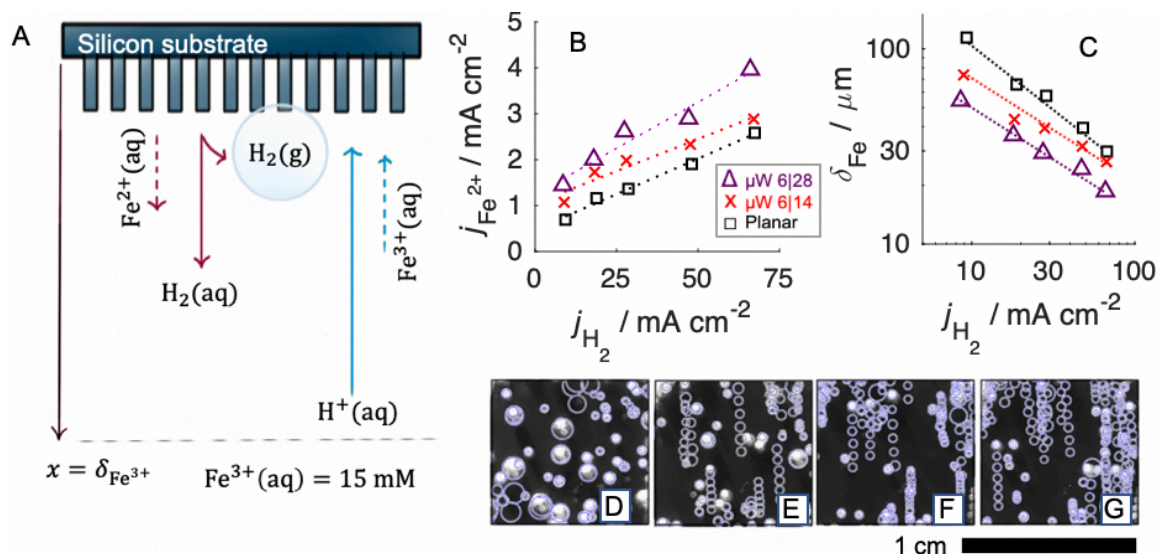


Figure 6.6: (A) Scheme of experimental procedure for diffusion-limited current experiments (B) Diffusion-limited current density measured via spectrophotometric determination of Fe²⁺(aq) from 15 mM Fe³⁺(aq) in 0.50 M H₂SO₄(aq), as a function of current density towards the HER, for various cathodes. Inverted ($\alpha = 15^\circ$) planar, μ W 6|28, and μ W 6|14 electrodes are represented as black squares, purple triangles, and red x's respectively, with dotted guidelines. (C) Length of the concentration boundary layer, assuming planar diffusion with the surface concentration of Fe²⁺ approaching zero. (D-G) Representative traces of gas bubbles at an inverted ($\alpha = 15^\circ$) μ W 6|14 electrode passing -10 (D), -30 (E), -50 (F), and -70 mA cm⁻² (G) sampled over 0.100 s and superimposed over a single image.

To calculate the concentration boundary layer thickness, δ_{Fe} , from J_{Fe} , the diffusion boundary layer was approximated as a continuous, stagnant layer (**Equation 6.2**):

$$\frac{J_O}{nF} = \frac{D_O}{\delta_O} [C_O^* - C_O|_{x=0}] \quad (6.2)$$

where D_O is the diffusion coefficient of the oxidized species, $n = -1$, F is Faraday's constant, C_O^* is the bulk concentration of the oxidized species and $C_O|_{x=0}$ is the concentration at the surface. Values for δ_{Fe} at inverted n⁺-Si/Ti/Pt microwire array electrodes, as

calculated from J_{Fe} , were inversely proportional to $|J_{H_2}|$ and were between 30 μm and 100 μm across the range of current densities relevant to a solar fuels device. (**Figure 6.5C**). For an inverted ($\alpha = 15^\circ$) μW 6|14 electrode operated at $|J_{H_2}| = 10, 30, 50, 70 \text{ mA cm}^{-2}$, representative traces of gas bubbles were sampled over 0.100 s and superimposed over a single image (**Figure 6.6D-G**). The total gas coverage was not sensitive to current density (**Figure 6.2**), but increases in current density resulted in a substantially larger fraction of bubbles that were in motion.

6.3.4 *Electrochemical impedance of bubble films*

The effect of the gas bubble layers on the series resistance, R_{sol} , as a function of time was probed via galvanostatic impedance measurements. The measurements were performed at a frequency for which the impedance was predominantly determined by the solution resistance. Planar electrodes at $\alpha = 15^\circ$ exhibited η and R_{sol} values that were more variable with time than the corresponding values for planar electrodes at $\alpha = 90^\circ$. For planar electrodes at $|J_{H_2}| = 30 \text{ mA cm}^{-2}$, the additional ohmic drop, ΔE_{ohm} , due to the presence of a bubble layer was $22 \pm 7 \text{ mV}$ at $\alpha = 15^\circ$ and was $6 \pm 2 \text{ mV}$ at $\alpha = 90^\circ$. Figure 5.6 presents chronopotentiometric traces obtained at planar Pt cathodes as a function of α and $|J_{H_2}|$, overlaid with an envelope representing one standard deviation in ΔE_{ohm} calculated from measurements of R_{sol} . The variance in ΔE_{ohm} accounted for the majority of the fluctuations in the electrode potential with time.

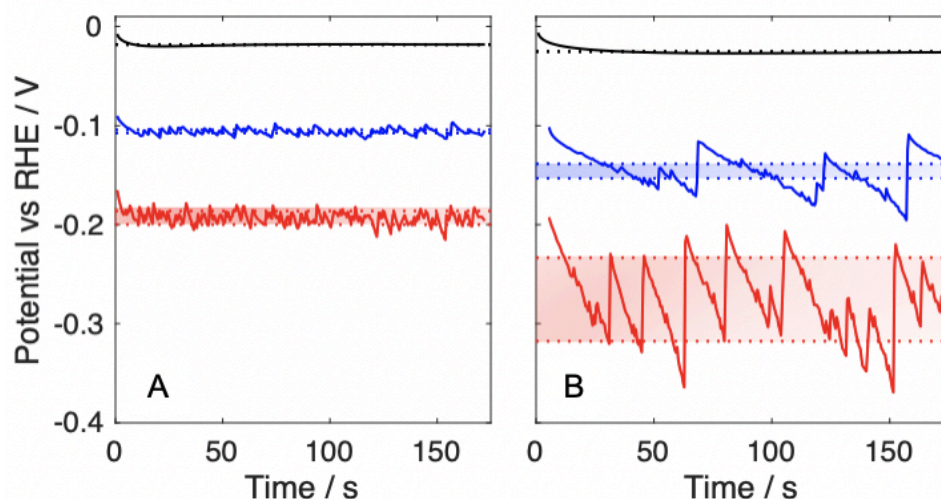


Figure 6.7: Potential versus time data for a planar Pt electrode at (A) 90° orientation and (B) 15° orientation at 10, 30, and 70 mA cm⁻², black, blue, and red lines, respectively. Shaded regions represent the average potential \pm one standard deviation in the potential, corrected for ohmic drop, measured via galvanostatic impedance.

Figure 6.8A presents the average current density vs. overpotential relationship for planar, μ W 6|14, and μ W 3|11 n⁺-Si/Ti/Pt electrodes, respectively, at $\alpha = 15^\circ$ after correcting for ΔE_{ohm} due to the R_{sol} value measured at 0.0 V versus RHE. For comparison, the ideal current vs. overpotential behavior predicted for a planar Pt surface with a Tafel slope of 29 mV dec⁻¹, in the absence of mass-transport limitations, is shown as a continuous black line (**Equation 6.3**):

$$\eta_{Tafel} = a + b \log_{10} |J| \quad (6.3)$$

where a and b are the empirical Tafel parameters. Planar n⁺-Si/Ti/Pt electrodes exhibited substantial deviations from Tafel behavior at all current densities, and the J - η relationship was linear rather than exponential. n⁺-Si/Ti/Pt μ W array electrodes exhibited decreased deviations from Tafel behavior and the J - η relationship was exponential for $|J_{H_2}| < 50$ mA cm⁻².

The relative contributions of ohmic drop, catalyst surface area, and increased concentration of $H_2(aq)$ can be separated into different classes of overpotentials. At an electrode surface covered by gas bubbles at constant current, an additional overpotential required due to an increase in effective current density at sites not covered by gas bubbles is given by **Equation 6.4**:

$$\eta_h = b \log_{10}[A/A'] \quad (6.4)$$

where η_h represents the hyperpolarization, and is dependent on the ratio of A to the remaining active area A' .⁹ In the absence of gas bubbles, accumulation of $H_2(aq)$ in the boundary layer shifts the local reversible hydrogen electrode potential as predicted by a Nernstian relationship (**Equation 6.5**):

$$\eta_c = 2.3 \frac{RT}{nF} \log[C_{H_2}|_{x=0}/C_{H_2}^*] \quad (6.5)$$

where R is the gas constant, F is Faraday's constant and n is the number of electrons involved in the reaction.

The measured ohmic drop contribution was compared to the resistance of a hypothetical layer of gas bubbles with a single thickness, L , and void fraction, f_g . The effective conductivity, K_m , of a mixed-phase layer was calculated from an equation originally proposed by Maxwell (**Equation 6.6**):

$$K_m = (1 - f_g)/(1 + \frac{f_g}{2}) \quad (6.6)$$

and used to estimate the additional ohmic drop during gas evolution (**Equation 6.7**):

$$\Delta E_{ohm} = \frac{iL(1-K_m)}{\kappa K_m} + \left[\frac{iL}{\kappa} \right] \quad (6.7)$$

where κ is the solution conductivity,²⁵ with the ohmic drop present in the absence of gas bubbles contained within brackets, and $\Delta E'_{ohm}$ represents the remaining ohmic drop after removal of this term.^{9, 26}

The total potential drop between the cathode and reference electrode, following correction for the cell resistance, can be expressed by **Equation 6.8**:⁹

$$\eta_T = \Delta E'_{ohm} + \eta_{Tafel} + \eta_h + \eta_c \quad (6.8)$$

Equation 6.8 was used to simulate the J - η relationship of H₂-evolving cathodes as a function of varied f_g , L , and $C_{H_2(aq)}$.

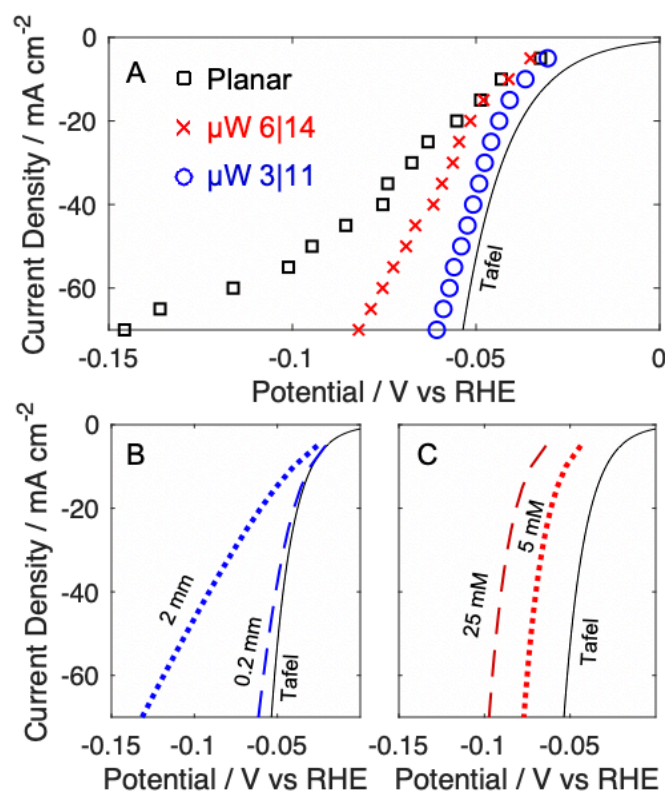


Figure 6.8: (A) Comparison of the steady-state J - E behavior for the HER for planar (black squares), μW 6|14 (red x's), and μW 3|11 electrodes (blue circles), in a downward configuration at $\alpha = 15^\circ$ in 0.50 M H₂SO₄(aq). (B) Comparison of the simulated J - η behavior of a Pt cathode covered by a 1 mm (dotted blue line) or a 3 mm thick (dashed blue line) close-packed bubble layer. (C) Comparison of the simulated J - η behavior of a Pt cathode in the presence of $C_{H_2(aq)} = 5$ and 25 mM, depicted as dotted and dashed red lines, respectively.

A quantitative comparison between the coverage of gas bubbles and the observed overpotentials was not performed, due to the difficulty of quantifying L at electrode surfaces that were covered by bubbles exhibiting diameters that varied with position and time. The peak weighted mean diameter of bubbles attached to planar and μW 3|11 electrodes at -30 mA cm^{-2} was 2 mm and 0.2 mm, respectively (**Figure 6.4**). Simulated J - E data for a hypothetical close packed layer of gas bubbles with these values of L are presented as **Figure 6.8B**. Increasing f_g from 0.3 to 0.6, near the limit for a single layer of hexagonally close-packed spheres, increased the overpotential at $|J_{H_2}| = 30 \text{ mA cm}^{-2}$, η_{30} , by 5%, whereas increasing the thickness of the bubble layer to 3 mm increased η_{30} by 44% (**Figure 6.8C**). Relative to a bare Pt surface, decreases of 30% and 60% in the catalyst surface area due to bubble coverage led to an increase in η_{30} of 9% and 23%, respectively. Increasing the local $C_{H_2(aq)}$ to 5 mM or 25 mM led to an increase in η_{30} of 53% and 102%, respectively, relative to a cathode with a surface $C_{H_2(aq)} = 0.78 \text{ mM}$.

6.4 Discussion

The capillary forces due to electrolyte infilling of μW arrays exceed the buoyant forces due to gravity, and thus prevent obstruction of μW electrode surfaces by bubbles, regardless of α . Microwire array electrodes exhibit smaller adhesive forces towards gas bubbles than planar electrodes, leading to more rapid release of bubbles and more stable η_T . Adhesion of individual gas bubbles could occur exclusively at the top face of microwires, known as the Cassie-Baxter state, or additionally at the sidewalls and substrate, known as the Wenzel state.²⁷ Mutually similar departure diameters were measured via high-speed microscopy for μW 6|14 and μW 6|28 electrodes, which is inconsistent with an

adhesion process that depends on the internal surface area of the microwire array but is consistent with adhesion being dominated by the top-facing area of an individual microwire or defect site. Results from this work extend a prior study that demonstrated stabilized photoelectrochemical behavior of Si μ W and nanowire array electrodes at $\alpha = 90^\circ$ due to a reduced θ relative to planar electrodes,²²⁻²³ and additionally indicate that μ W electrodes exhibit chronopotentiometric behavior that is insensitive to θ even against buoyant force vectors directed antiparallel to the surface normal.

Increases to $C_{H_2(aq)}$ and L constituted the largest relative contributions to increased values of η_T at small and large $|J_{H_2}|$, respectively. At $|J_{H_2}| = 30 \text{ mA cm}^{-2}$ the effects of θ on f_g and A^* contributed $< 10 \text{ mV}$ of added overpotential. These results are consistent with the differing chronopotentiometric behavior of μ W array and planar electrodes having mutually similar θ values. These observations suggest that the primary factor leading to stabilized potentials at μ W array electrodes is a reduced gas layer thickness due to a decreased departure diameter for H_2 bubbles. Further decreases in bubble layer thicknesses may be obtained by decreasing the tip radius of the μ W array,²⁴ for example by utilization of Si microcone arrays that have been developed to minimize optical reflection losses at photoelectrodes.²⁸⁻²⁹

Electrodes prepared from μ W 6|14 arrays had the highest areal filling fraction of microwires and exhibited the lowest θ values at all current densities. The differences in θ for inverted μ W 6|14 and μ W 6|28 electrode geometries were caused by variations in the density of nucleation sites on the surface, as opposed to differences in the departure diameters of bubbles (**Figure 6.5**). Values of θ measured at μ W 6|28 arrays were very sensitive to the orientation of the electrode, whereas μ W 6|14 arrays exhibited low values

of N and θ at $\alpha = 15^\circ$ (Figures 6.3-6.4). Due to the high free-energy barrier to forming a new gas-liquid interface, gas bubbles predominately formed at cavities located at defects or at small gas bubbles left behind during release of macroscopic bubbles (**Figures 6.5, 6.9**).³⁰ The increased filling fraction at $\mu\text{W } 6|14$ electrodes, relative to $\mu\text{W } 6|28$ and $\mu\text{W } 3|11$ electrodes, prevented isolated bubbles from propagating new nucleation sites upon detachment, and resulted in lower values of N and θ . Studies on isolated Pt nanoelectrodes have shown that $C_{\text{H}_2(\text{aq})} > 0.1 \text{ M}$ are required to form new heterogeneous nuclei.⁴ The behavior of the $\mu\text{W } 6|14$ electrodes at macroscale electrode areas in this work demonstrates that only a few such nuclei are needed across the surface to generate sufficient convection to prevent further nucleation. Differences in θ between inverted $\mu\text{W } 6|14$ and $\mu\text{W } 6|28$ electrodes are caused by emergent properties of the microwire arrays that are specific to testing conditions relevant to operation of a solar fuels device, and moreover would not be readily predicted from the characteristics of bubble formation on individual, isolated Si microwires.

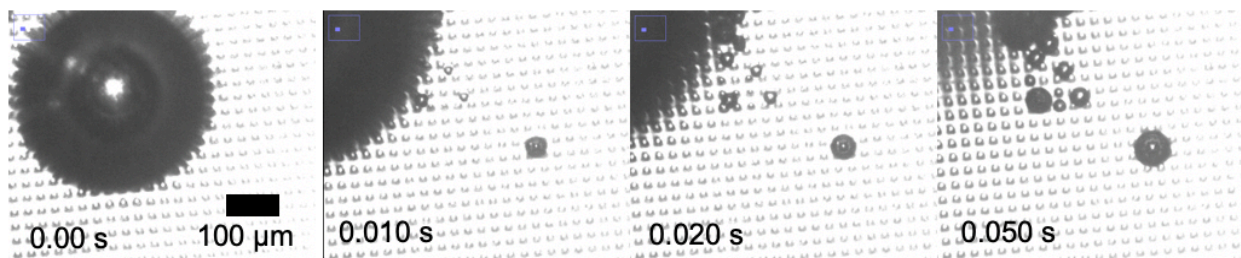


Figure 6.9: High speed microscope images recorded at an upward-facing $\mu\text{W } 6|28$ electrode evolving H_2 in $0.50 \text{ M H}_2\text{SO}_4(\text{aq})$. The departing gas bubble at 0.010 s left multiple nucleation sites within the microwire array.

In the absence of bubbles, accumulation of $\text{H}_2(\text{aq})$ at the surface leads to a substantial η_C , which shifts the J - η characteristic towards more negative potentials while

maintaining an exponential relationship between J and η . Such behavior is consistent with the comparison of steady-state overpotentials at downward-facing μ W-array electrodes (**Figure 6.3B-D**) suggesting that a decrease in θ led to an increase in $C_{H_2(aq)}$ at the surface due to the absence of liquid-gas interfaces available to collect $H_2(aq)$. This result is consistent with the observation of increased overpotentials at -10 mA cm^{-2} for upward-facing electrodes (**Figure 6.2A-B**), which readily detached bubbles, in comparison to downward-facing electrodes. At low $|J_{H_2}|$ the voltage loss due to $\Delta E'_{ohm}$ is small in comparison to η_C so the presence of bubbles consequently led to a lower $C_{H_2(aq)}$ and lower η_T at downward-facing electrodes. The linear relationship between R and $t^{1/2}$ for bubbles on upward-facing microwire arrays demonstrated that bubble growth was controlled by transport of dissolved H_2 to the gas-liquid interface from a fluid volume comparable to the volume of gas bubbles,¹⁴² which displayed diameters greater by a factor of 10 than the length of individual microwires. In this respect, the growth behavior of bubbles on microwire arrays is physically similar to the growth behavior at a planar surface. Large dimensionless-growth coefficients were observed at upward-facing microwire array electrodes, which have been used to determine $C_{H_2(aq)}$ (**Figure 6.5**),³¹ however \tilde{b} values measured at $|J_{H_2}| > 10 \text{ mA cm}^{-2}$ were too large to ignore the effects of advection (**A.6**).³² Because η_C is inversely proportional to n , concentration overpotentials incurred during the oxygen-evolution reaction ($n = 4$) will be reduced relative to overpotentials during the HER ($n = 2$). Assuming that O_2 and H_2 exhibit similar degrees of supersaturation prior to nucleation,⁴⁻⁵ evolving O_2 on the top side of a solar-fuels device will lead to reduced total concentration overpotentials because low gas coverages on the top side of a device are

likely to lead to an increase in supersaturation of the electrochemical reaction product in the electrolyte.

Despite the physical obstruction of electrolyte responsible for mass transport of reactants and products, the generation of gas bubbles led to an increased $|J_O|$ in comparison to $|J_O|$ in a stagnant electrolyte (**Figure 6.6**). Assuming that the Faradaic efficiency for $H_2(g)$ evolution is not a strong function of J_{H_2} , over the range of 10-70 mA cm⁻²,³³ transport of $Fe^{3+}(aq)$ to the electrode surface was driven by volumetric displacement of electrolyte due to H_2 evolution (Figure 5.5B). Platinized Si μW arrays consistently exhibited larger $|J_{Fe}|$ values than planar n⁺-Si/Ti/Pt electrodes, regardless of gas bubble coverage, however the largest $|J_{Fe}|$ values were observed at the arrays that had the largest θ values. The relationship between δ and J_{H_2} is consistent with theoretical relationships for mass transport driven by microconvection or fluid penetration during individual bubble detachment, for which $\delta \sim J_{H_2}^{-1/2}$, as opposed to macroconvection driven by rising bubble films, for which $\delta \sim J_{H_2}^{-1/3}$.³⁴ Comparable values for δ have been measured via $Ce^{3+/4+}$ potentiometric titration for Pt foils at $\alpha = 90^\circ$ and 180° evolving $O_2(g)$ or $H_2(g)$ in 1.0 M $H_2SO_4(aq)$.³⁵ Previous investigations have inferred that surface roughness did not have substantial effects on δ or that the decreased δ was a function of the increased nucleation density.³⁶⁻³⁷ The results in this work, for electrodes with explicitly controlled microstructure, at $\alpha = 15^\circ$, and at current densities relevant to solar-fuels devices, demonstrate that surface adhesion and microconvection are the dominant independent variables controlling the mass transport properties of bubble films, as opposed to nucleation density or buoyancy-driven convection. For electrodes oriented against \hat{g} in a stagnant

electrolyte, the generation of bubbles increases reactant influx and product efflux such that mass transport will not limit device performance.

6.5 Conclusion

Collectively, the results obtained for inverted cathodes suggest that efficient and stable electrochemical generation of gases can be obtained via control of the electrode microstructure. When oriented against gravity, the low adhesive force and high number density of bubbles at $\mu\text{W } 3|11$ and $\mu\text{W } 6|28$ electrodes leads to thin layers of gas bubbles that exhibit a low resistance, yielding electrochemical behavior that is insensitive to θ . Notably, μW electrodes that maintained a high N and θ exhibited the largest mass transport coefficients and lowest η . In contrast, at J_{H_2} values relevant to solar-fuel device operation in unconcentrated sunlight, the absence of bubbles is not desirable, and produced deleterious increases in η that were comparable to the kinetic overpotential exhibited by a Pt catalyst. Moreover, planar $n^+\text{-Si/Ti/Pt}$ electrodes exhibited the worst performance of all of the electrodes studied herein, because they produced large, stationary bubbles that generated the least convection and consequently contributed to a large ΔE_{ohm} . Optimal electrode morphologies and geometries will therefore nucleate bubbles across the surface, keeping $C_{H_2(aq)}$ in near-equilibrium with $H_2(g)$ at the operating pressure, and will moreover be structured to quickly detach bubbles from the surface, thereby minimizing the thickness of the gas layer and maximizing local convection. Microcavities and surface functionalization can facilitate nucleation to maintain low $C_{H_2(aq)}$ values at the surface.³⁸⁻

³⁹ Further studies should assess whether electrodes that include membranes containing hydrophobic polymer chains also result in sufficient capillary forces to prevent infilling of

gas bubbles, and/or whether further surface modification of the microstructure can prevent such infilling. Although the gas coverage of Pt catalysts was not a substantial contributor to the total η , additional studies should investigate the electrochemical behavior of microstructured electrodes covered by catalysts with increased Tafel slopes, relative to Pt catalyzing the HER, to determine how gas coverage affects less active but earth-abundant catalysts for the HER and OER. The electrodes in this work were degenerately doped and therefore insensitive to the optical effects of gas coverage. Experiments on upward-facing, photoactive microwire electrodes are needed to determine whether high coverages of small gas bubbles are suitable for efficient collection of sunlight.